Chinese Chemical Letters 33 (2022) 2501–2506

Contents lists available at ScienceDirect

Chinese Chemical Letters

journal homepage: www.elsevier.com/locate/cclet

Boron difluoride formazanate dye for high-efficiency NIR-II fluorescence imaging-guided cancer photothermal therapy

Hanming Dai[a,1], Zijin Cheng[a,1], Tian Zhang[a], Weili Wang[a], Jinjun Shao[a,*], Wenjun Wang[b], Yongxiang Zhao[c], Xiaochen Dong[a,*], Liping Zhong[c,*]

[a] Key Laboratory of Flexible Electronics (KLOFE) & Institute of Advanced Materials (IAM), Nanjing Tech University (NanjingTech), Nanjing 211800, China
[b] School of Physical Science and Information Technology, Liaocheng University, Liaocheng 252059, China
[c] National Center for International Biotargeting Theranostics, Guangxi Key Laboratory of Biotargeting Theranostics, Collaborative Innovation Center for Targeting Tumor Theranostics, Guangxi Medical University, Nanning 530021, China

ARTICLE INFO

Article history:
Received 4 October 2021
Revised 23 November 2021
Accepted 26 November 2021
Available online 1 December 2021

Keywords:
NIR-II nanotheranostics
Boron difluoride formazanate
Fluorescence imaging
Photothermal therapy
Phototheranostics

ABSTRACT

The small molecular second near-infrared (NIR-II, 1000–1700 nm) dye-based nanotheranostics can concurrently combine deep-tissue photodiagnosis with *in situ* phototherapy, which occupies a vital position in the early detection and precise treatment of tumors. However, the development of small molecular NIR-II dyes is still challenging due to the limited electron acceptors and cumbersome synthetic routes. Herein, we report a novel molecular electron acceptor, boron difluoride formazanate (BDF). Based on BDF, a new small molecular NIR-II dye BDF1005 is designed and synthesized with strong NIR-I absorption at 768 nm and bright NIR-II peak emission at 1034 nm. *In vitro* and *in vivo* experiments demonstrate that BDF1005-based nanotheranostics can be applied for NIR-II fluorescence imaging-guided photothermal therapy of 4T1 tumor-bearing mice. Under 808 nm laser irradiation, tumor growth can be effectively inhibited. This work opens up a new road for the exploitation of NIR-II small molecular dyes for cancer phototheranostics.

Cancer (malignant tumor) remains a severe threat to human life and health [1]. The traditional medical diagnostic techniques cannot effectively identify early-stage tumors [2]. Thus, once the cancer is diagnosed, it may be at an advanced stage [3]. The current clinical cancer treatment methods lack accuracy, which will result in normal tissue damage or irreversible side effects [4,5]. This is not only the reason for the limited curative effect but also why the tumor is prone to recurrence and metastasis after treatment. Given the above situation, developing more precise and efficient cancer theranostics will have far-reaching significance to improve the survival rate of patients and defeat cancer.

Fluorescence imaging (FLI) has shown superior promise for detecting early-stage tumors over conventional diagnosis due to the benefits of high sensitivity and strong specificity [6]. However, the strong absorption of endogenous substances and tissue light scattering in the first near-infrared (NIR-I, 700–900 nm) region make NIR-I FLI cannot penetrate deep tissues to detect deep-seated lesions, which limits its biomedical applications [7,8]. The NIR-II FLI has emerged and aroused tremendous interest in both fundamental research and clinical practice to increase the imaging depth. Due to the negligible tissue absorption, scattering, and auto-fluorescence in the NIR-II region, NIR-II FLI exhibits excellent spatio-temporal resolution, high signal-to-noise ratio, and deep penetration, which makes it a unique advantage in early tumor detection compared to NIR-I FLI and traditional diagnosis [9–11]. Photothermal therapy (PTT) has been regarded as a novel and alternative therapeutic mode to conventional clinical treatment owing to its non-invasive, area controllable, and negligible drug resistance [12–14]. In principle, PTT is a physical process of light-to-heat conversion. The photothermal agent under irradiation will absorb light energy and then dissipate energy to create *in situ* hyperthermia *via* intense intramolecular chemical bond rotation or intermolecular collisions [15–18]. The local hyperthermia ($\geq$ 43 °C) will in turn directly destroy cell membranes and organelles and ultimately promote cell necrosis [19,20]. The combination of NIR-II FLI and PTT will be of great benefit in reducing iatrogenic injuries and side effects, thereby improving the efficiency and accuracy of cancer diagnosis and treatment.

* Corresponding authors.
E-mail addresses: iamjjshao@njtech.edu.cn (J. Shao), iamxcdong@njtech.edu.cn (X. Dong), zhong_liping@163.com (L. Zhong).
[1] These authors contributed equally to this work.

https://doi.org/10.1016/j.cclet.2021.11.079
1001-8417/

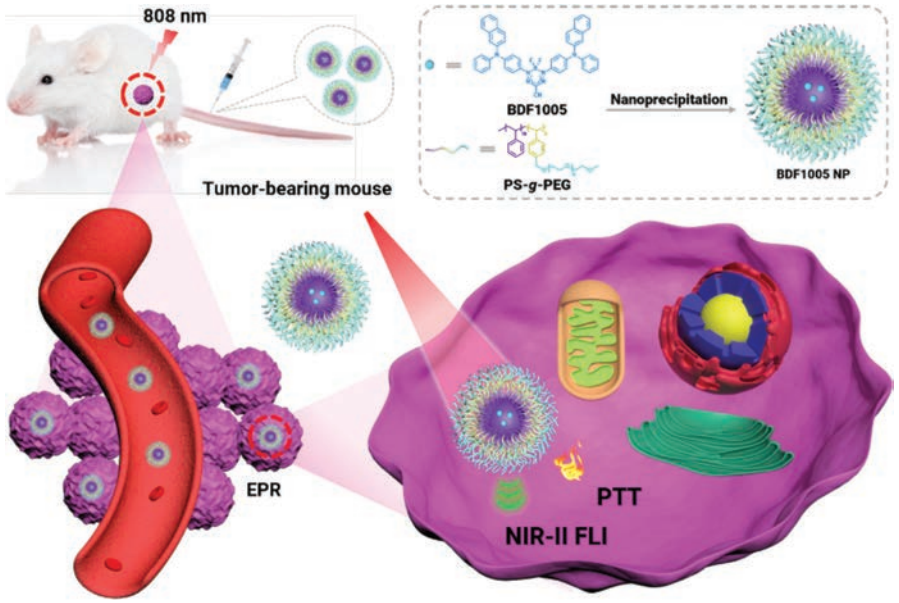

Scheme 1. Schematic illustration of BDF1005 NPs for cancer phototheranostics.

NIR-II nanotheranostics simultaneously performs NIR-II imaging and phototherapy in a single nanoplatform, which plays a vital role in the early diagnosis and simultaneous precision treatment of cancer [21–24]. Currently, the research of NIR-II nanotheranostics mainly focuses on inorganic nanomaterials (such as gold nanostructures, rare-earth-doped nanoparticles, quantum dots), semiconducting polymers, and organic small molecules [25–28]. However, the obstacles of poor biocompatibility, metabolic difficulties, and potential long-term biological toxicity make the clinical transformation of inorganic nanomaterials worrying [29]. Although semiconducting polymers have good biocompatibility, their molecular weight and structures often have uncertain problems [30–33]. In contrast, organic small molecules are favored due to their batch-to-batch reproducibility, well-defined structure, high purity, and excellent biosafety [34–36]. At present, the vast majority of the developed small molecular NIR-II dyes are still limited to traditional acceptors, such as benzobisthiadiazole (BBT), cyanine, dipyrromethane boron difluoride (BODIPY), diketopyrrolopyrrole (DPP), for the construction of donor-acceptor-donor (D-A-D) scaffold [37–40]. Additionally, the synthesis steps of them are numerous, which leads to insufficient diversity and difficulty of exploitation.

Herein, we reported a new type of electron acceptor boron difluoride formazanate (BDF), and designed and synthesized a novel organic small molecular NIR-II dye BDF1005 *via* D-A-D strategy. By using the amphiphilic polymer poly(styrene-*co*-chloromethyl styrene)-*graft*-poly(ethylene glycol) (PS-*g*-PEG) as the matrix, the NIR-II organic nanotheranostics was prepared *via* the nanoprecipitation method. Compared with most NIR-II organic nanotheranostics that have been reported, BDF1005 NPs had excellent NIR-II fluorescence properties and high photothermal conversion efficiency. Given the significant theranostic performance, BDF1005 NPs were further applied for NIR-II FLI-guided PTT on 4T1 tumor-bearing mice (Scheme 1), and showed good ability to inhibit tumor growth. We hope this work can provide new insights for the development of organic small molecular dye-based NIR-II nanotheranostics and the promotion of tumor precision treatment.

Small molecular dye, BDF1005, was facilely prepared through a four-step reaction (Fig. 1). Its chemical structure was well characterized by nuclear magnetic resonance (NMR) and high-resolution mass spectroscopy (HRMS), which were presented in the Supporting information (Figs. S8–S10 in Supporting information). In the chemical structure of BDF1005, *N,N*-diphenylnaphthalen-2-amine unit served as the donor and together with the acceptor BDF to construct the D-A-D scaffold, which could extend the π-conjugation and promote the intramolecular charge transfer (ICT) for the bathochromic shift of the absorption and emission spectra [41,42].

As shown in Fig. 2a, BDF1005 presented a broad absorption profile covering from 500 nm to 950 nm, with an absorption peak at 768 nm in dichloromethane. Under 808 nm laser photoirradiation, BDF1005 in dichloromethane showed bright fluorescence emission in the NIR-II region with an emission peak at 1034 nm (Fig. 2b). Due to the good electron-donating capability of *N,N*-diphenylnaphthalen-2-amine unit and the strong electron-withdrawing ability of BDF core, a narrow optical energy gap (E_g) of 1.86 eV was achieved for BDF1005 in dichloromethane (Fig. 2c and Fig. S1 in Supporting information). Additionally, the absorption and fluorescence spectra of BDF1005 in toluene, chloroform, and *n*-hexane were also recorded (Fig. S2 in Supporting information). And the absorption peak at 732 nm was observed for BDF1005 in *n*-hexane, showing a hypsochromic shift of over 30 nm compared to that in toluene, chloroform, and dichloromethane. Furthermore, BDF1005 presented broad NIR-II fluorescence profiles ranging from 850 nm to 1400 nm in the four organic solvents. Interestingly, two fluorescence peaks at 863 nm and 960 nm could be found for BDF1005 in *n*-hexane. Subsequently, the solvatochromic Stokes shift was studied through the Lippert-Malaga plot for quantitative analysis of the dipole moment change ($\Delta\mu$) between ground and excited states. And the dipole moment change ($\Delta\mu$) of BDF1005 was calculated to be 3.049 Debye from the plot slope, indicating an efficient intramolecular charge transfer (ICT) of the D-A-D architecture.

The fluorescence emission property of molecular aggregates of BDF1005 was further studied by regulating the hexane fraction (f_w) of toluene/*n*-hexane mixtures (Fig. S3 in Supporting information). As the *n*-hexane fraction (f_w) varying from 0% to 90%, the emission intensity increased steadily, showing a phenomenon of aggregation-enhanced emission, which could be due to the bulky structure of the electron donors (Fig. S4 in Supporting information) [43].

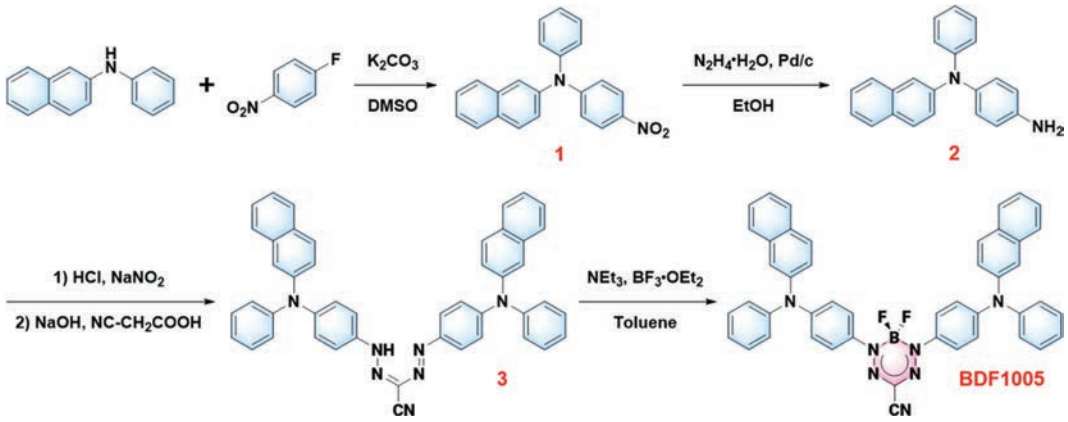

Fig. 1. Synthesis route of NIR-II dye BDF1005.

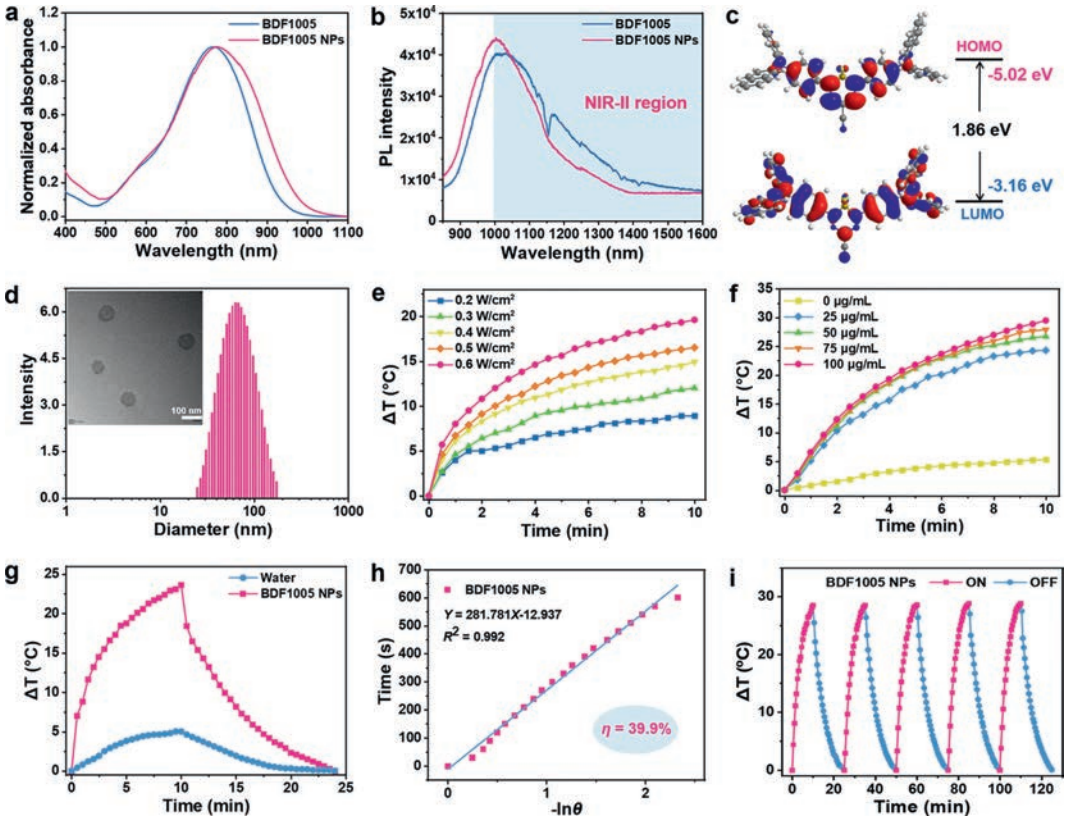

Fig. 2. (a) Normalized UV-vis-NIR absorption spectra and (b) fluorescence spectra of BDF1005 in dichloromethane and BDF1005 NPs in water. (c) Molecular orbital amplitude plots of HOMO/LUMO energy levels of BDF1005. (d) DLS profiles of BDF1005 NPs aqueous dispersions, and corresponding TEM image (inset). (e) Photothermal performance of BDF1005 NPs (80 μg/mL) as a function of power density under 10 min photoirradiation of 808 nm laser. (f) Photothermal performance of BDF1005 NPs (100 μg/mL) as a function of concentration under 10 min photoirradiation of 808 nm laser (1.0 W/cm^2). (g) Photothermic heating curves of BDF1005 NPs (100 μg/mL) and water under 10 min photoirradiation of 808 nm laser (0.8 W/cm^2), followed by naturally cooling to room temperature. (h) Relationship between time and $-\ln\theta$ θ is the driving force of temperature. (i) Photothermal stability of BDF1005 NPs upon 808 nm laser irradiation of 1.0 W/cm^2 for five alternate on/off cycles.

The biocompatible and water-soluble nanoparticles (NPs) were fabricated by encapsulating the small molecular dye BDF1005 into the amphiphilic polymer PS-*g*-PEG. The polymeric PS-*g*-PEG was prepared according to previous report [44], and its characterization was shown in the Supporting information (Fig. S11 and Table S2 in Supporting information). In the aqueous solution, the absorption of BDF1005 NPs showed a bathochromic shift with the peak at 775 nm (Fig. 2a). Although the fluorescence emission peak of BDF1005 NPs in an aqueous solution displayed a hypochromic shift to 1005 nm, the fluorescence still maintained a high intensity (Fig. 2b), as indicated that BDF1005 NPs could be used as the contrast agent for NIR-II FLI. BDF1005 NPs with uniform spherical shape were demonstrated by the transmission electron microscopy (TEM) and had a diameter of 65 nm (Fig. 2d), which matched well with the hydrodynamic size of 72.4 ± 30.3 nm from dynamic light scattering (DLS) measurement.

The fluorescence QY of BDF1005 in dichloromethane was studied at first, and it is determined to be 0.69%, by taking commercial dye IR1061 as the reference (Fig. S5 in Supporting information). In the aqueous solution, BDF1005 NPs still maintained a high fluorescence QY of 0.44%, and was one of the highest among the previously reported results [37,45]. It is probably due to the large steric hindrance of the periphery triarylamine unit, which will limit the rotation of the dye molecules to a certain extent and significantly impede the aggregation caused quenching (ACQ) effect. In addition, the fluorescence lifetime of BDF1005 NPs was measured to

be 0.41 ns through the time-correlated single-photon counting (TCSPC) technique (Fig. S6 in Supporting information). And the radiative decay rate (K_r) and non-radiative decay rate (K_{nr}) of BDF1005 NPs were calculated to be 1.07 × 10^7 s^{-1} and 1.54 × 10^7 s^{-1}, respectively.

To evaluate the photothermal performance of BDF1005 NPs, the temperature variation of NPs aqueous solution was recorded under the irradiation of 808 nm laser with different power densities (Fig. 2e). Different concentrations of NPs aqueous solution were also irradiated by 808 nm laser (Fig. 2f). In the first two minutes of irradiation, the temperature rose rapidly, then slowly increased until it reached the plateau, showing power density and concentration dependence. The excellent photothermal performance could be attributed to the high molar absorption coefficient (2.15 × 10^4 L mol^{-1} cm^{-1}) of BDF1005 at 808 nm. Then, the NPs aqueous solution was irradiated with 808 nm laser for 10 min to heat and then naturally cooled for another 15 min to room temperature. Under 10 min of irradiation, BDF1005 NPs could increase by about 25.0 °C (Fig. 2g), which indicated the excellent photothermal effect. The photothermal conversion efficiency (η) of BDF1005 NPs was determined to be 39.9% (Fig. 2h), which was higher than the most reported NIR-II small molecular dyes (such as H2a-47 [46], BPN-BBTD [47], BPBBT [48] and SQP [49]). Even after five cycles of "on-off" photoirradiation, there was almost no apparent change in the maximum temperature variation (Fig. 2i), which showed excellent photothermal stability for BDF1005 NPs.

Given the excellent photothermal conversion efficiency of BDF1005 NPs, cell experiments were further performed to evaluate their dark toxicity and phototoxicity *in vitro*. And different cell lines of MCF-7, 4T1, and HACAT were applied to investigate the cytotoxicity of BDF1005 NPs *via* MTT (3-(4,5-dimethyl-2-thiazolyl)-2,5-diphenyl-2*H*-tetrazolium bromide) assay. In different concentrations of BDF1005 NPs, cell viabilities were negligibly affected without laser irradiation. Even at a high concentration of 50 μg/mL, three kinds of cells could still maintain a high cell viability of about 90% (Fig. 3a), which indicated good biocompatibility and low dark toxicity of BDF1005 NPs. 4T1 tumor cells were further used to evaluate the phototoxicity of BDF1005 NPs. Upon 808 nm irradiation for 6 min, significant cell ablation could be observed; remarkably, at the concentration of 45 μg/mL, the cell viability of 4T1 tumor cells significantly dropped below 10% (Fig. 3b), indicating the excellent cell ablation performance for BDF1005 NPs. The half maximal inhibitory concentration (IC_{50}) value was calculated to be 24.4 μg/mL. To show the ability of photothermal ablation more intuitively, 4T1 tumor cells were double-stained by using calcein AM and PI. Without irradiation, the cells only emitted green fluorescence. On the contrary, a significant red fluorescence could be observed after irradiation (Fig. 3c), which indicated that most cells had been ablated. These results demonstrated that BDF1005 NPs possessed the potential to be photothermal agents.

At first, the fluorescence imaging penetration depth was studied. The fat emulsion injection was used to simulate the biological tissues. As shown in Fig. 3d, for BDF1005 NPs, even if the thickness was increased to 6 mm, a clear NIR-II fluorescence image could be observed, owing to the long fluorescence emission wavelength of BDF1005 NPs [50]. Next, the *in vivo* NIR-II fluorescence imaging performance of BDF1005 NPs was studied in 4T1 tumor-bearing Balb/c mice, which was an established subcutaneous tumor model of murine breast cancer. A single dose of BDF1005 NPs aqueous solution (200 μg/mL, 100 μL) was administrated *via* tail vein injection. The whole-body image of mice was continuously recorded under 808 nm laser irradiation. At a different time, NIR-II fluorescence at the tumor site was marked from background tissue. As shown in Fig. 4a, the fluorescence intensity gradually became strong at 24 h post-injection, which was attributed to the gradual accumulation of BDF1005 NPs at the tumor site *via* the enhanced

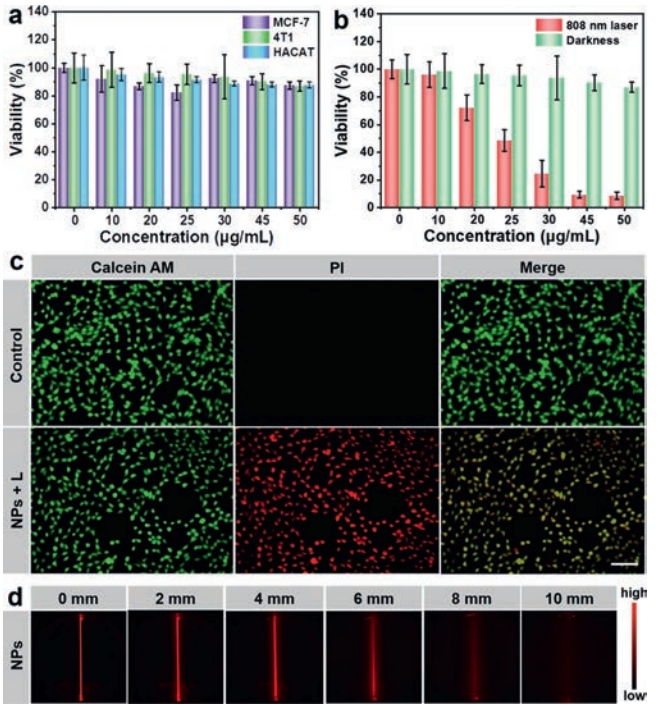

Fig. 3. (a) Cell viability of different cell lines treated with varying concentrations of BDF1005 NPs, measured by MTT under dark. (b) Cell viability of 4T1 cells treated with different concentrations of BDF1005 NPs measured by MTT (808 nm, 1.0 W/cm^2). (c) Fluorescence images of 4T1 cells co-stained with calcein AM (live cells, green) and PI (dead cells, red) upon the addition of BDF1005 NPs with/without irradiation (808 nm, 1.0 W/cm^2). Scale bar: 100 μm. (d) NIR-II fluorescence images of BDF1005 NPs at different depths (0, 2, 4, 6, 8 and 10 mm) under 808 nm laser irradiation.

permeation and retention (EPR) effect. At 24 h post-injection, the brightness of the tumor site reached the maximum, showing the effective accumulation of BDF1005 NPs in the tumor tissues. The *ex-vivo* biodistribution of BDF1005 NPs was further investigated by detecting the fluorescence intensity of normal organs and tumor tissues after 24 h post-injection. As shown in Fig. 4b, only liver, spleen, and tumor tissue presented strong fluorescence intensity, indicating that BDF1005 NPs had good biosafety and might excrete *via* liver and spleen.

Furthermore, the NIR-II FLI of mouse hind-limb blood vasculature was accessed with BDF1005 NPs. The BDF1005 NPs aqueous solution (200 μg/mL, 100 μL) was injected directly into mice through the tail vein. After 5 min administration, the right hind-limb vasculature could be visualized from the background tissue upon 808 nm laser irradiation (Fig. 4c). The signal-to-background ratio (SBR) was determined to be ~1.34 by Gaussian fit (Fig. 4d). The results demonstrated that BDF1005 NPs were promising to guide tumor treatment.

Inspired by the above results, the photothermal performance of BDF1005 NPs *in vivo* was explored in the 4T1 tumor-bearing mouse model. All animals were treated according to the Guide for Care and Use of Laboratory Animals, approved by the Animal Experimentation Ethics Committee of Nanjing Tech University. After 24 h administration (200 μg/mL, 100 μL), the tumor site was irradiated with 808 nm laser (1.0 W/cm^2) for 6 min, and the photothermal images were recorded every 2 min. In the group with BDF1005 NPs injection, the temperature of the tumor site rapidly increased from 35.7 °C to 48.7 °C within 6 min (Fig. 5a), which was high enough to ablate 4T1 tumor cells. By contrast, the temperature of the PBS injection group only rose 2.6 °C (Fig. 5b). The results indicated the excellent photothermal effect *in vivo* of BDF1005 NPs.

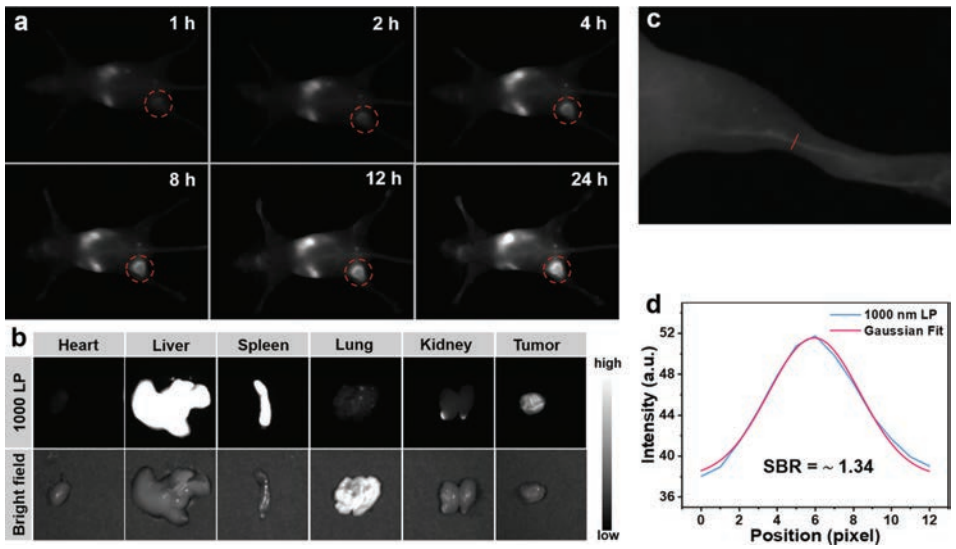

Fig. 4. (a) NIR-II fluorescence images of the 4T1 tumor site at different times after tail-vein injection of BDF1005 NPs under 808 nm laser excitation. (b) *Ex vivo* biodistribution of BDF1005 NPs in the heart, liver, spleen, lung, kidneys, and tumor at 24 h post-injection under 808 nm laser excitation. (c) NIR-II fluorescence images of the mouse hind limb vasculature. (d) The intensity profile of the mouse hind limb vasculature (blue line) and Gaussian fit intensity profile (red line).

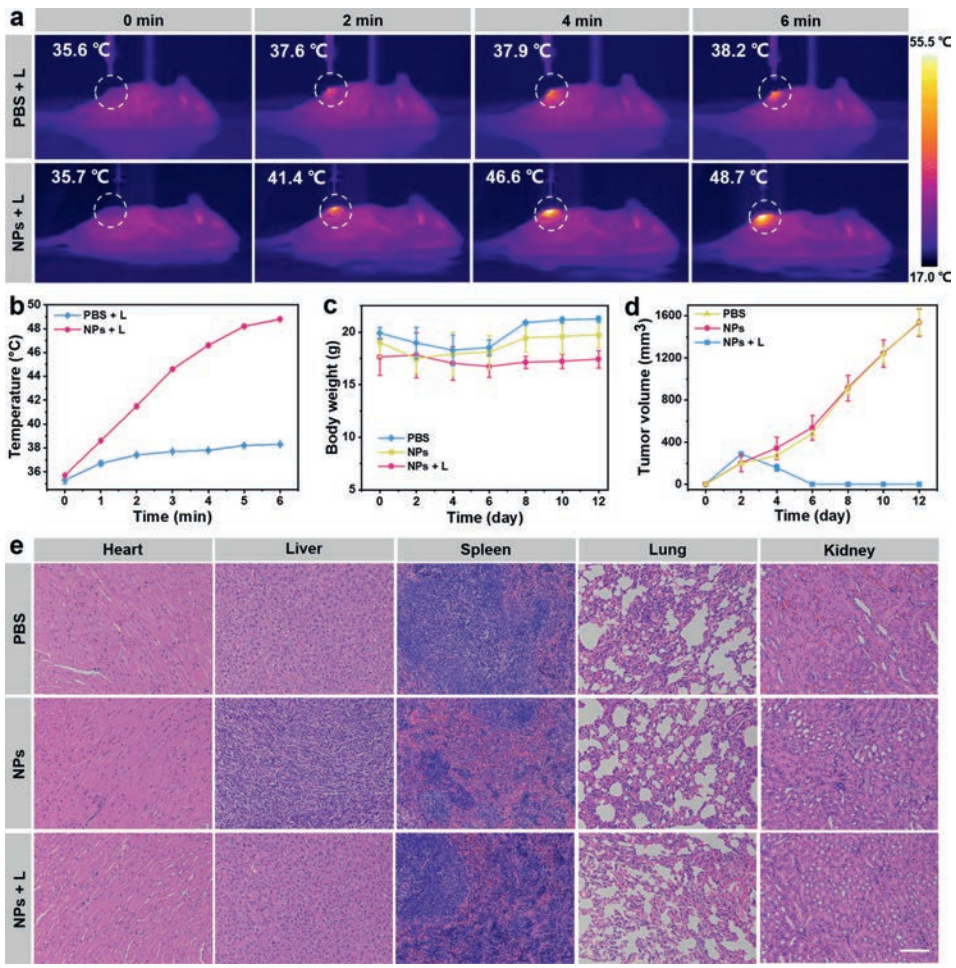

Fig. 5. (a) *In vivo* photothermal images of the 4T1 tumor-bearing mice after intravenous injection of saline and BDF1005 NPs under 808 nm laser irradiation (1.0 W/cm^2). (b) The temperature curve of the tumor site under 808 nm laser irradiation treated with saline and BDF1005 NPs. (c) Changes in the bodyweight of the mice in different groups during treatment. (d) Tumor volume changes from the mice in different groups. (e) H&E staining of the major organs (heart, liver, spleen, lung, and kidney) for different groups after 12 days treatment of BDF1005 NPs. Scale bar: 100 μm.

Encouraged by the excellent photothermal activity *in vivo*, the imaging-guided phototherapeutic efficacy of BDF1005 NPs was further evaluated. The 4T1 tumor-bearing mice were randomly divided into three groups (3 mice per group): (I) PBS, (II) BDF1005 NPs, and (III) BDF1005 NPs + L. On the first day, BDF1005 NPs aqueous solution (200 μg/mL, 100 μL) was intravenously injected into each mouse in group II and group III. For group I, each mouse was injected with 100 μL of PBS. During the 24 days of treatment, the mice's bodyweight and tumor volume were recorded every two days. As shown in Fig. 5c, no noticeable bodyweight loss was observed in the three groups' mice, suggesting the excellent biocompatibility and biosafety of the phototherapy. Meantime, the tumor volumes of BDF1005 NPs + L group were drastically reduced after the first photoirradiation (Fig. 5d), as indicated that the tumor growth could be effectively inhibited. On the contrary, the tumors proliferated for the PBS group and BDF1005 NPs only group. After 12 days of treatment, the tumors of the mice treating with BDF1005 NPs with photoirradiation could be eliminated (Fig. S7 in Supporting information), demonstrating the excellent phototherapeutic efficacy.

Finally, the hematoxylin and eosin (H&E) staining was carried out on normal organ tissues. As shown in Fig. 5e, no noticeable pathological abnormalities were observed in major organs (heart, liver, spleen, lung, and kidney) of all groups, which once again proved the good biosafety of the phototherapeutic treatment.

In summary, a small molecular NIR-II dye BDF1005 with D-A-D architecture was reasonably designed and readily synthesized based on the novel acceptor boron difluoride formazanate (BDF). Subsequently, by encapsulating BDF1005 dye molecules with amphiphilic polymer PS-*g*-PEG, the water-soluble BDF1005 NPs were prepared with an excellent fluorescence quantum yield of 0.44% in the aqueous solution and a high photothermal conversion efficiency of 39.9%. Under the navigation of NIR-II fluorescence imaging, the area-controllable and precise photothermal therapy effectively suppressed and eliminated tumors in a short treatment time. Therefore, our work provided a promising approach to develop novel small molecular NIR-II dye for phototheranostics.

Declaration of competing interest

The authors declare that they have no known competing financial interests or personal relationships that could have appeared to influence the work reported in this paper.

Acknowledgments

The work was supported by the National Natural Science Foundation of China (No. 61775095), Natural Science Foundation of Jiangsu Province (No. BK20200092), Jiangsu Province Policy Guidance Plan (No. BZ2019014), Natural Science Foundation of Shandong Province (No. ZR2020KB018), and 'Taishan scholars' construction special fund of Shandong Province. We are also grateful to the High-Performance Computing Center in Nanjing Tech University for supporting the computational resources.

Supplementary materials

Supplementary material associated with this article can be found, in the online version, at doi:10.1016/j.cclet.2021.11.079.

References

[1] H. Sung, J. Ferlay, R. Siegel, et al., CA Cancer J. Clin. 71 (2021) 209–249.
[2] Y. Su, B. Yu, S. Wang, H. Cong, Y. Shen, Biomaterials 271 (2021) 120717.
[3] J. Chen, H. Pan, Z. Wang, et al., Chem. Commun. 56 (2020) 2731–2734.
[4] Z. Cao, L. Feng, G. Zhang, et al., Biomaterials 155 (2018) 103–111.
[5] D. Voshart, J. Wiedemann, P. van Luijk, L. Barazzuol, Cancers 13 (2021) 367.
[6] Y. Chen, L. Li, W. Chen, H. Chen, J. Yin, Chin. Chem. Lett. 30 (2019) 1353–1360.
[7] Y. Cai, Z. Wei, C. Song, et al., Chem. Soc. Rev. 48 (2019) 22–37.
[8] L. Lu, B. Li, S. Ding, et al., Nat. Commun. 11 (2020) 4192.
[9] S. Wang, B. Li, F. Zhang, ACS. Cent. Sci. 6 (2020) 1302–1316.
[10] J. Li, Y. Liu, Y. Xu, et al., Coord. Chem. Rev. 415 (2020) 213318.
[11] Z. Hu, C. Fang, B. Li, et al., Nat. Biomed. Eng. 4 (2020) 259–271.
[12] F. An, Z. Yang, M. Zheng, et al., J. Nanobiotechnol. 18 (2020) 49.
[13] Y. Xiao, F. An, J. Chen, et al., Small 15 (2019) 1903121.
[14] G. Feng, G. Zhang, D. Ding, Chem. Soc. Rev. 49 (2020) 8179–8234.
[15] S. Li, Q. Deng, Y. Zhang, et al., Adv. Mater. 32 (2020) e2001146.
[16] S. Liu, Y. Li, R. Kwok, J. Lam, B. Tang, Chem. Sci. 12 (2021) 3427–3436.
[17] H. Jung, P. Verwilst, A. Sharma, et al., Chem. Soc. Rev. 47 (2018) 2280–2297.
[18] D. Xi, M. Xiao, J. Cao, et al., Adv. Mater. 32 (2020) e1907855.
[19] H. Sun, Q. Zhang, J. Li, et al., Nano Today 37 (2021) 101073.
[20] P. Zhao, H. Jiang, D. Su, et al., Mol. Med. Rep. 11 (2015) 327–332.
[21] Y. Cai, W. Si, W. Huang, et al., Small 14 (2018) e1704247.
[22] J. Zhou, L. Rao, G. Yu, et al., Chem. Soc. Rev. 50 (2021) 2839–2891.
[23] S. Ling, X. Yang, C. Li, et al., Angew. Chem. Int. Ed. 59 (2020) 7219–7223.
[24] H. Dai, X. Wang, J. Shao, et al., Small 17 (2021) e2102646.
[25] Y. Yang, X. Fan, L. Li, et al., ACS Nano 14 (2020) 2509–2521.
[26] D. Zhao, X. Yang, X. Hou, et al., J. Mater. Chem. B 7 (2019) 2484–2492.
[27] Y. Zhang, T. Song, T. Feng, et al., Nano Today 35 (2020) 100987.
[28] L. Li, C. Shao, T. Liu, et al., Adv. Mater. 32 (2020) e2003471.
[29] A.L. Antaris, H. Chen, K. Cheng, et al., Nat. Mater. 15 (2016) 235–242.
[30] L. Li, X. Dong, J. Li, J. Wei, Dye. Pigment. 183 (2020) 108756.
[31] X. Zhen, K. Pu, X. Jiang, Small 17 (2021) e2004723.
[32] H. Xu, D. Zhang, J. Li, J. Bioresour. Bioprod. 4 (2019) 177–182.
[33] H. Huang, L. Mao, Z. Li, et al., J. Bioresour. Bioprod. 4 (2019) 231–241.
[34] S. Zhu, R. Tian, A. Antaris, X. Chen, H. Dai, Adv. Mater. 31 (2019) e1900321.
[35] Q. Wang, X. Niu, L. Yang, et al., Mater. Chem. Front. 5 (2021) 5689–5697.
[36] Q. Yu, X. Huang, T. Zhang, et al., Chem. Res. Chin. Univ. 37 (2021) 951–959.
[37] H. Dai, Q. Shen, J. Shao, et al., Innov. 2 (2021) 100082.
[38] Q. Zhang, Q. Wang, X. Xu, et al., Dye. Pigment. 193 (2021) 109480.
[39] H. Ma, C. Liu, Z. Hu, et al., Chem. Mater. 32 (2020) 2061–2069.
[40] L. Bai, P. Sun, Y. Liu, et al., Chem. Commun. 55 (2019) 10920–10923.
[41] Z. Cheng, T. Zhang, W. Wang, et al., Chin. Chem. Lett. 32 (2021) 1580–1585.
[42] G. He, J. Shao, Y. Li, et al., Phys. Chem. Chem. Phys. 18 (2016) 6789–6798.
[43] J. Qi, X. Duan, W. Liu, et al., Biomaterials 248 (2020) 120036.
[44] H. Wan, J. Yue, S. Zhu, et al., Nat. Commun. 9 (2018) 1171.
[45] Q. Wang, Y. Dai, J. Xu, et al., Adv. Funct. Mater. 29 (2019) 1901480.
[46] X. Zeng, Y. Xiao, J. Lin, et al., Adv. Healthc. Mater. 7 (2018) e1800589.
[47] N. Alifu, A. Zebibula, J. Qi, et al., ACS Nano 12 (2018) 11282–11293.
[48] S. Gao, G. Wei, S. Zhang, et al., Nat. Commun. 10 (2019) 2206.
[49] P. Sun, Q. Wu, X. Sun, et al., Chem. Commun. 54 (2018) 13395–13398.
[50] L. Tu, Y. Xu, Q. Ouyang, X. Li, Y. Sun, Chin. Chem. Lett. 30 (2019) 1731–1737.